Atomic-level modulation of local coordination environment at Fe single-atom sites for enhanced oxygen reduction

Jing Sun [a,1], Hui Xue [a,1], Lanlu Lu [b,1], Mingbin Gao [c], Niankun Guo [a], Tianshan Song [a], Hongliang Dong [d], Jiangwei Zhang [a,c,*], Limin Wu [a,e,*], Qin Wang [a,*]

a College of Chemistry and Chemical Engineering, Inner Mongolia University, Hohhot 010021, PR China
b National Facility for Protein Science, Shanghai Advanced Research Institute, Chinese Academy of Sciences, Shanghai 201210, PR China
c National Engineering Laboratory for Methanol to Olefins, Dalian Institute of Chemical Physics, Chinese Academy of Sciences, Dalian 116023, PR China
d Center for High Pressure Science and Technology Advanced Research, Shanghai 201203, PR China
e Department of Materials Science and State Key Laboratory of Molecular Engineering of Polymers, Fudan University, Shanghai 200433, PR China

ABSTRACT

Single-atom catalysts (SACs) have aroused extensive attention due to their ultrahigh activity and selectivity. However, precisely regulating and designing the coordination microenvironment of SACs to optimize the catalytic efficiency remains a great challenge. Here, a facile ionic liquid (IL) modification strategy is creatively proposed to obtain N and P dual-coordinated Fe single atoms with N unsaturated coordination on pre-designed $Fe_{SAC}-N_4/C$ sites. The using a hydrophobic IL can alter the binding affinity of O_2, maintain a higher O_2 concentration at the catalyst interface, and protect Fe single atom sites from surface oxidation and methanol toxicity. Theoretical calculation indicates that this unique coordination and the N vacancy can tailor the electronic structure of the metal atoms and alter the charge distribution at the coordination structures, thus improving the oxygen reduction reaction performance. This study offers an effective approach for accurately controlling the coordination electronic structure and interface environment of SACs at room temperature.

1. Introduction

Single-atom catalysts have proved to be the most effective candidates for driving oxygen reduction reactions (ORR) in fuel cells and metal-air batteries because of their maximum atomic utilization and high electrocatalytic activity [1–4]. M-N-C synthesized by metal-organic frameworks (MOFs) have customizable and well-defined structures that offer unique advantages in precisely constructing the desired materials [5–7]. To date, MOFs-derived SACs have received extensive attention. However, due to the limitations in electrocatalytic activity and stability, further commercial applications of SACs are still difficult [8–10]. Therefore, improving the activity and stability of SACs through rational design and structural regulation has become a research hotspot.

The SACs are stabilized through coordination interactions with the support. Therefore, from the perspective of coordination chemistry, modulating the local coordination environment is a sensible tactic to improve the ORR property [11,12]. Tuning the number and type of coordination atoms can greatly change the electronic and geometric structure of the active metal centers in SACs [13,14]. Some recent studies have shown that the symmetric plane and saturated coordination structure are detrimental to the adsorption and activation of ORR-related catalysts, consequently limiting the ORR kinetics and active [15]. Introducing heteroatoms (P, S etc.) with different atomic radius and electronegativity in the center of the active metal can modulate the coordination atomistic structure, which is a clever method to destroy the symmetry of electronic density [16,17]. Strategies used so far are almost limited to the one-step pyrolysis of targeted heteroatoms-doped MOF precursors, and the doped heteroatom may interfere the formation of SAC. At the same time, the long-term pyrolysis process leads to the loss of N content, and the complex synthesis parameters, such as pyrolysis temperature, metal loading, seriously limit the flexibility and versatility of this strategy [18,19]. Although greatly diligently have been devoted to control the microenvironmental structure of SACs by introducing heteroatoms, there is still a lack of reasonable guidance for achieving accurate coordination numbers without interfering with the formation of single atoms.

---

* Corresponding authors at: College of Chemistry and Chemical Engineering, Inner Mongolia University, Hohhot 010021, PR China.
E-mail addresses: jwz@imu.edu.cn (J. Zhang), lmw@fudan.edu.cn (L. Wu), qinwang@imu.edu.cn (Q. Wang).
1 These authors contributed equally to this work.
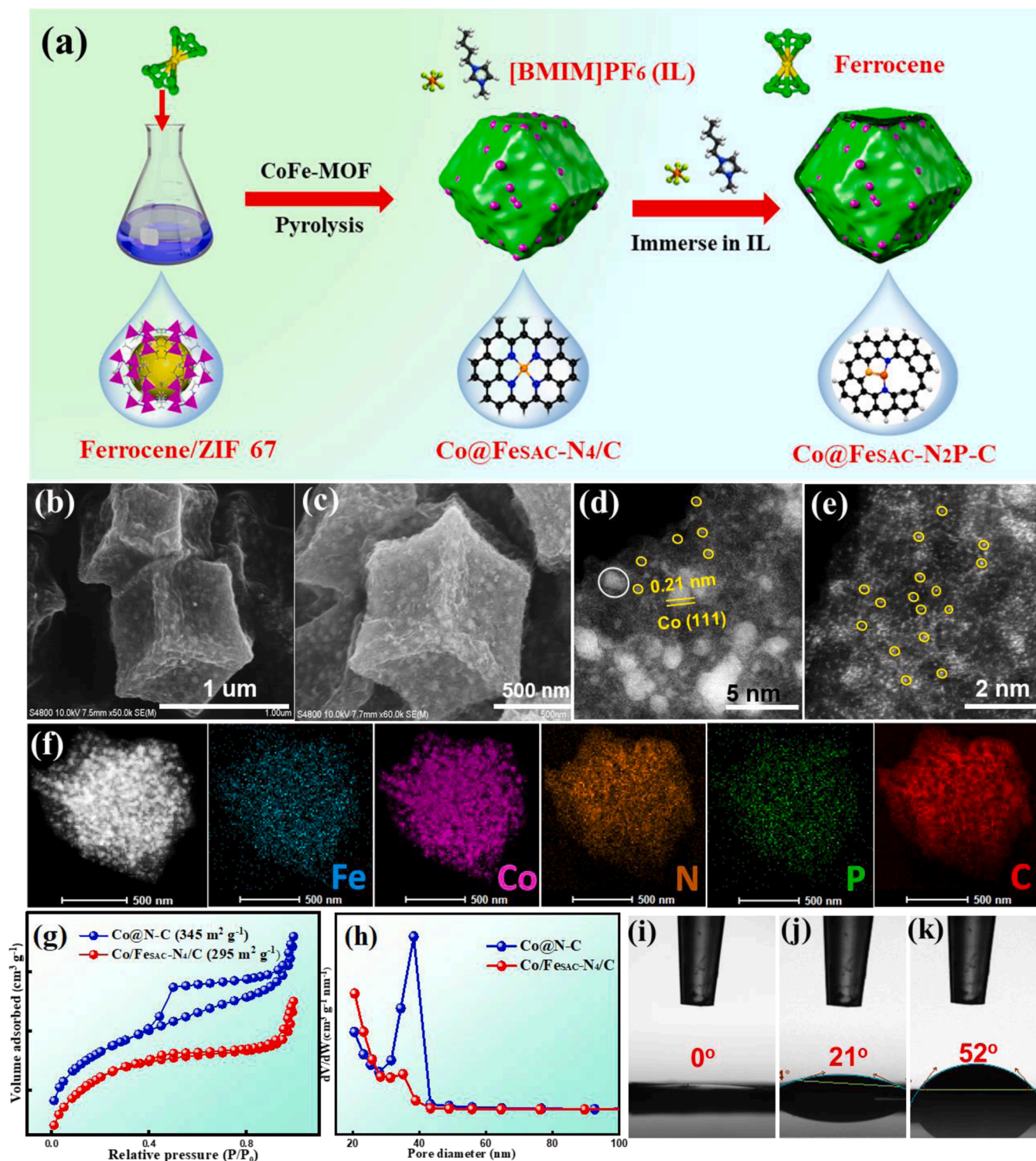
Fig. 1. a) Schematic illustration of the synthetic strategy for the Co@Fe_SAC-N2P/C; SEM images of b) Co@Fe_SAC-N4/C, c) Co@Fe_SAC-N2P/C; d-e) HAADF-STEM images of Co@Fe_SAC-N2P/C; f) HAADF-STEM and elemental mapping of Co@Fe_SAC-N2P/C; g-h) N_2 adsorption-desorption isotherms and the corresponding pore size distribution; static water contact angle of Co@Fe_SAC-N4/C immersed in different contents of IL i) 0 mg, j) 40 mg, and k) 70 mg.

In addition, modulating the hydrophobic/hydrophilic microenvironment of SACs can alter the binding affinity of O_2, biasing a higher O_2 to concentrate at the catalyst surface, thus increasing O_2 residence time and trial frequency of ORR [20]. Combined with DFT and Poisson Boltzmann calculations, Jinnouchi et al. proposed that the interface water itself may lead to the blockage of the active site of the catalyst [21]. And increasing the hydrophobicity of the catalytic material surface

would protect active sites by repelling water molecules from the product and aqueous electrolyte [22]. Therefore, it is highly desired to develop an effective heteroatom introduction approach to accurately control the coordination structure of single-atom metal, while optimizing the interface microenvironment to create a hydrophobic surface.

ILs are a type of room-temperature molten organic salts with extremely low vapor pressure, high stability, and strong solvency, which

can provide more heteroatoms (N, P, F, and B) and create hydrophobic microenvironment at catalyst surfaces [23]. Herein, we creatively put forward a facile approach, by immersing Co@Fe$_{SAC}$-N$_4$/C into a hydrophobic IL ([BMIM]PF$_6$) (1-butyl-3-methylimidazolium hexafluorophosphate), to achieve Co@Fe$_{SAC}$-N$_2$P/C mixed unsaturated coordination structure. This approach achieves the function of regulating the coordination environment and hydrophobicity of the SAC simultaneously, without disturbing the formation of SACs. The incorporation of P and N unsaturated coordination can tailor the electronic structure of the metal atoms and alter the charge distribution at the coordination structures, thus improving the oxygen reduction reaction performance [24,25]. More importantly, the hydrophobic surface can maintain a higher O$_2$ concentration at the catalyst interface, and owing to the protection by the hydrophobic surface, the active sites of SACs are not in direct contact with the alkaline solution, effectively repelling the toxicity of methanol and the water during ORR. As a result, by introducing [BMIM]PF$_6$ to Co@Fe$_{SAC}$-N$_4$/C catalyst, a significant improvement has been gained in the ORR performance. The optimized Co@Fe$_{SAC}$-N$_2$P/C shows an outstanding ORR activity with a half-wave potential of 0.92 V and a long stability with 40,000 cycles, exceeding that of the Pt/C and most non-precious metal ORR electrocatalysts. Furthermore, the Zn-air battery assembled by Co@Fe$_{SAC}$-N$_2$P/C catalyst delivers a higher power density of 179 mW·cm^{-2}, which is much higher than Pt/C+IrO$_2$ (116 mW·cm^{-2}). Density functional theory (DFT) indicates that Fe atomic sites coordinated by N and P atoms (Fe-N$_2$P) and N unsaturated coordination (N vacancy) are preferable to the formation of OOH* , resulting in fast reaction kinetics and good ORR efficiency. This study provides a convenient and effective approach for accurately controlling coordination electronic structure and interface environment of SACs and optimizing ORR performance.

2. Experimental section

2.1. Synthesis of ZIF-67 and CoFe-MOF

In a typical synthesis of ZIF-67, Co(NO$_3$)$_2$·6H$_2$O (7.5 mmol, 2.184 g) and 2-methylimidazole (60 mmol, 4.926 g) were dissolved in 40 mL methanol. Then, two solutions were mixed with vigorous stirring for 3 min at room temperature. The as-prepared purple precipitate was washed with methanol three times and dried at 50 °C. CoFe-MOF was synthesized with the same procedure of ZIF-67 except that the extra ferrocene (3 mmol, 0.558 mg) was added.

2.2. Synthesis of Co@N-C and Co@Fe$_{SAC}$-N$_4$/C

The Co@N-C and Co@Fe$_{SAC}$-N$_4$/C catalysts were obtained by sintering the ZIF-67 and CoFe-MOF powder to 800 °C in a quartz tube furnace under N$_2$ at a heating rate of 5 °C·min^{-1} and keeping at this temperature for 2 h, respectively.

2.3. Synthesis of IL-modified Co@Fe$_{SAC}$-N$_4$/C catalysts (Co@Fe$_{SAC}$-N$_2$P/C)

70 mg [BMIM]PF$_6$ was diluted with deionized water to make IL solution. The Co@Fe$_{SAC}$-N$_4$/C catalyst was added into IL solution and ultrasonic bath was conducted for 10 min to ensure the uniform dispersion of the Co@Fe$_{SAC}$-N$_4$/C. Then, the mixed slurries were kept at room temperature for 8 h. And, the sample was collected by centrifuging, washed several times with distilled water and ethanol, and dried at 50 °C under vacuum, finally affording Co@Fe$_{SAC}$-N$_2$P/C sample.

2.4. Electrochemical measurements

All electrochemical and electrocatalytic tests were conducted on a CHI760E (Shanghai, China) electrochemical workstation in a three-electrode configuration. The rotating disk electrode (RDE) loading the catalyst ink (3 μL) was used as the working electrode, new saturated calomel electrode as the reference electrode and carbon rod as the counter electrode, respectively. To prepare catalyst inks, 5 mg catalyst was ultrasonically dispersed in 500 μL water + ethanol (1:1) and 20 μL 5 wt% Nafion solution for 30 min to form a homogeneous ink (0.01 mg/μL). Then, 3 μL of the ink was dropped on the surface of the rotating disk electrode and dried at room temperature naturally. The linear sweep voltammetry (LSV) polarization curves were performed at −0.9 and 0.2 V (vs RHE) in O$_2$-saturated 0.1 M KOH solution at the scan rate of 5 mV·s^{-1} with different rotating rates (400–2500 rpm). The H$_2$O$_2$ yield and the electron transfer number (n) was obtained by RRDE measurements.

2.5. Zinc–air battery tests

The zinc-air battery was assembled with the Zn foil, Co@Fe$_{SAC}$-N$_2$P/C loading carbon paper, and 6 M KOH aqueous solutions were used as the anode, cathode, and the electrolyte, respectively. The as-prepared catalyst (20 mg) was ultrasonically dispersed in water + ethanol (1000 μL) containing Nafion solution (20 μL) for 6 h. The catalyst ink was then drop-casted on the carbon paper (2 cm^2) with a catalyst loading of 0.5 mg·cm^{-2}. At a current density of 5.0 mA·cm^{-2}, the stability of constant current charge-discharge cycles of Co@Fe$_{SAC}$-N$_2$P/C was measured in a LAND system. The polarization curves of the assembled zinc-air cell were recorded using LSV on the electrochemical platform CHI760E.

3. Results and discussion

3.1. Structure characterization

Fig. 1a schematically illustrates the synthetic procedure of Co@Fe$_{SAC}$-N$_2$P/C. In brief, the CoFe-MOF precursors were prepared by mixing solution of ferrocene, Co^{2+}, and 2-methylimidazole in methanol. After pyrolysis of CoFe-MOF under N$_2$ at 800 °C, typical Fe-N$_4$/C SACs materials with Co nanoparticles exposed on the surface of dodecahedron were obtained (Co@Fe$_{SAC}$-N$_4$/C). Further, Co@Fe$_{SAC}$-N$_4$-C catalysts were immersed into ILs to obtain Co@Fe$_{SAC}$-N$_2$P/C mixed unsaturated coordination catalyst. The morphology of the obtained catalysts was characterized by scanning electron microscopy (SEM) and transmission electron microscopy (TEM). In the mixed methanol solution of Co^{2+} and 2-methylimidazole, the Co-MOF of regular dodecahedron with the size of ∼ 1 μm is formed (Fig. S1a). After the addition of ferrocene, the resulting morphology of CoFe-MOF is almost the same as the Co-MOF (Fig. S1b). Upon pyrolysis of CoFe-MOF at 800 °C, Co@Fe$_{SAC}$-N$_4$/C retains the initial polyhedral shape, while the surface becomes rougher with the presence of obvious nanoparticles (Fig. 1b). After immersing Co@Fe$_{SAC}$-N$_4$/C catalyst into a hydrophobic IL, the morphology of Co@Fe$_{SAC}$-N$_2$P/C remains basically unchanged, indicating that the modification of IL does not change the morphology of catalyst (Fig. 1c). The TEM images further reveal the polyhedral morphology and the uniform dispersion of Co nanoparticles of Co@Fe$_{SAC}$-N$_2$P/C (Fig. S2a–c). The HRTEM of Co@Fe$_{SAC}$-N$_2$P/C images exhibit clear-defined lattice fringes with D-spacings of 0.21 nm, pointing to the (111) planes of the Co (Figs. S2d, 1d). As shown in the HAADF-STEM image of Co@Fe$_{SAC}$-N$_2$P/C (Fig. 1d–e), high density isolated bright dots associated with single Fe atoms (highlighted in yellow boxes) are obviously observed around the Co nanoparticles and evenly dispersed on the carbon layer. Elemental Mapping of Co@Fe$_{SAC}$-N$_2$P/C reveals the homogeneous dispersion of Co, Fe, N, P, and C. The existence of P indicates the uniform adsorption of IL into the Co@Fe$_{SAC}$-N$_2$P/C carbon matrix (Fig. 1f). On the basis of N$_2$ sorption isotherms, BET surface area of Co@N-C and Co@Fe$_{SAC}$-N$_4$/C are 345 and 295 m^2·g^{-1}, respectively (Fig. 1g). The pore sizes are distributed at 38 and 21 nm, respectively, suggesting a mesoporous structure for both Co@N-C and Co@Fe$_{SAC}$-N$_4$/C (Fig. 1h). The decrease of surface area for Co@Fe$_{SAC}$-N$_4$/C indicates the ferrocene is filling the
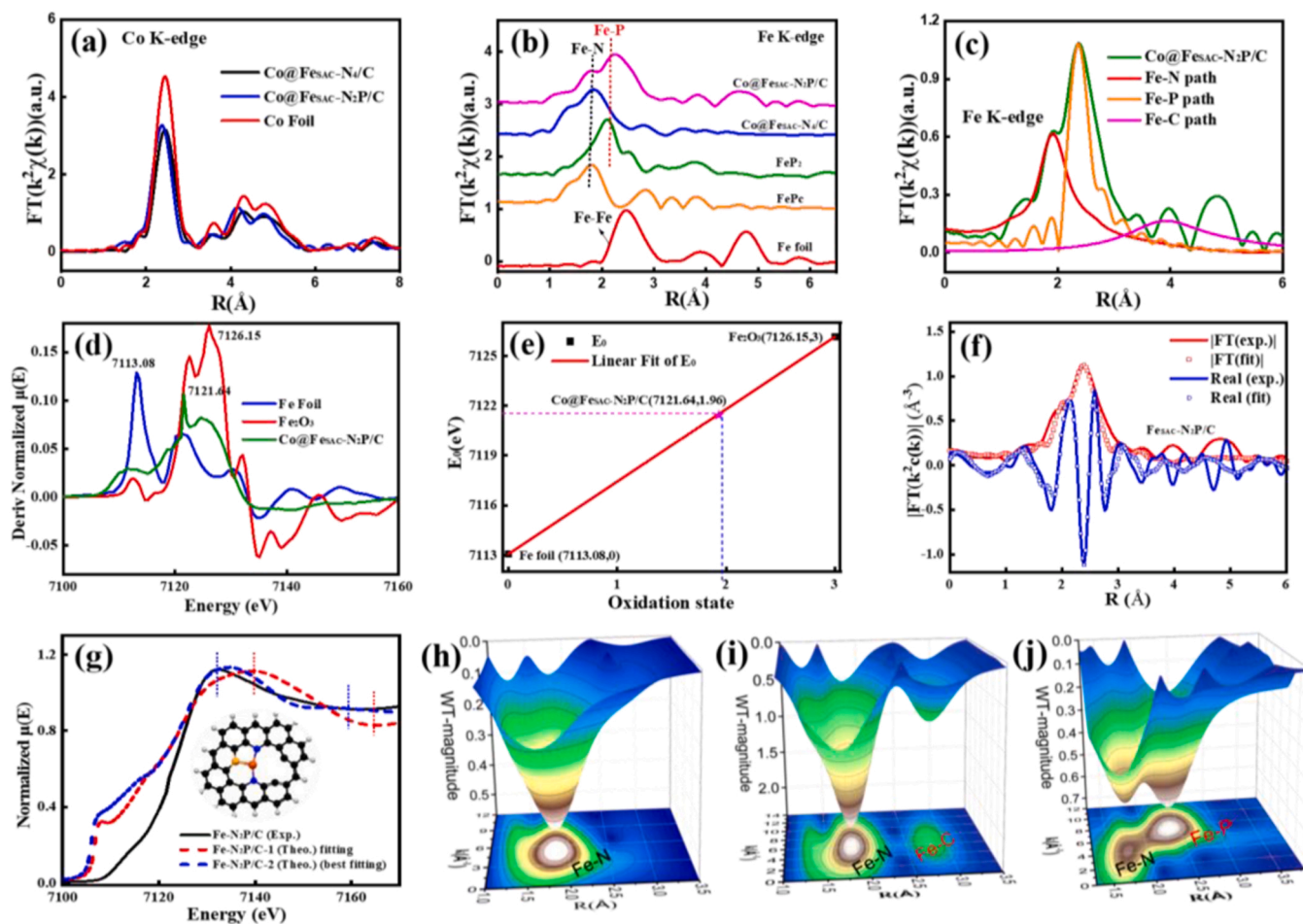
Fig. 2. Phase-corrected Fourier transformed EXAFS $k^2\chi(k)$ data of a) Co and b) Fe K-edge; c) the scattering path of Co@Fe$_{SAC}$-N$_2$P/C Fe K-edge; d) first derivative of Fe K-edge of Co@Fe$_{SAC}$-N$_2$P/C, e) precise oxidation state determination of Co@Fe$_{SAC}$-N$_2$P/C by linear fitting calibration; f) $\chi(R)$ space spectra fitting curve of Fe K-edge of Co@Fe$_{SAC}$-N$_2$P/C; g) Comparison of Fe K-edge XANES spectra of Fe$_{SAC}$-N$_2$P/C and theoretical XANES spectra calculated with different structural configuration; WT-EXAFS plots of h) FePc, i) Co@Fe$_{SAC}$-N$_4$/C, and j) Co@Fe$_{SAC}$-N$_2$P/C.

cavity of the Co@N-C [26]. The water contact angle of Co@Fe$_{SAC}$-N$_4$/C and Co@Fe$_{SAC}$-N$_2$P/C catalysts were measured to verify the changes in the hydrophilicity and hydrophobicity of the catalyst surfaces. The Fig. 1i–k show that the surface of the Co@Fe$_{SAC}$-N$_4$/C is completely wet with water, while Co@Fe$_{SAC}$-N$_4$/C immersion in 70 mg IL is the most hydrophobic, indicating that IL modification can cause the hydrophobicity change on the surface of Co@Fe$_{SAC}$-N$_4$/C.

The X-ray diffraction (XRD) patterns of Co@Fe$_{SAC}$-N$_4$/C and different amounts of IL-modified Co@Fe$_{SAC}$-N$_2$P/C samples are given in Fig. S3c–d. The diffraction peaks at 44.2°, 51.6°, and 75.9° can be accurately indexed into (111), (200), and (220) planes of Co (JCPDS#15–0806) (Fig. S3d). The other peak located at 26.0° accorded to (002) plane of C (JCPDS#41–1487) and without Fe-containing crystalline phases can be observed. At the same time, no trace of phase separation or other new phases are found after IL modification, which is in accord with the above TEM analysis (Fig. S3c).

In addition, the chemical composition and state atomic structures were investigated by X-ray photoelectron spectroscopy (XPS). The high-resolution Co 2p of Co@Fe$_{SAC}$-N$_2$P/C shows two peaks located at around 778.3 and 794.4 eV, corresponding to Co 2p$_{3/2}$ and Co 2p$_{1/2}$ peaks of Co^0 in the sample (Fig. S4a) [27]. The other peaks located at 780.5 eV and 797.1 eV are attributed to the 2p$_{3/2}$ and 2p$_{1/2}$ of Co^{2+} species (Fig. S4a) [28]. For XPS spectra of Fe 2p, the peaks at 713.5 and 733.3 eV correspond to 2p$_{3/2}$ and 2p$_{1/2}$ of Fe^{2+} species rather than metallic states (Fig. S4b) [29]. N 1 s for Co@Fe$_{SAC}$-N$_2$P/C exhibit three main peaks: pyridinic-N (398.5 eV), M-N (399.2 eV), and graphitic-N

(401.1 eV) (Fig. S4d) [30,31]. The binding energies of Fe 2p and M-N in Co@Fe$_{SAC}$-N$_2$P/C are positively shifted, compared to that of pristine Co@N-C and Co@Fe$_{SAC}$-N$_4$/C. On the contrary, the binding energy of Co 2p are negatively shifted, indicated that the IL modification can regulate the electronic structure of Co nanoparticles and Fe single atoms. And there are stronger electron coupling and interaction between Co and Fe single atoms [32]. Further, the electron coupling and interfacial electron interaction of the catalysts are indicated by ultraviolet photoelectron spectroscopy (UPS) (Fig. S4e). The UPS showed that the D-band center of Co@Fe$_{SAC}$-N$_4$/C shifted 0.16 eV relative to the Co@N-C because of electron transfer from the neighboring Fe atoms to the Co, which also indicates a strong electronic effect between Co and Fe single atoms.

The local structure and atomic state of Co@Fe$_{SAC}$-N$_4$/C and Co@Fe$_{SAC}$-N$_2$P/C were further conducted by X-ray absorption spectroscopy (XAS). The Co K-edge X-ray absorption near-edge structure (XANES) spectrum of Co@Fe$_{SAC}$-N$_4$/C and Co@Fe$_{SAC}$-N$_2$P/C overlap well with the Co foil, suggesting the valence state of Co is Co^0 (Fig. S5a) [33]. Co K-edge phase-corrected Fourier transforms EXAFS (FT-EXAFS) of Co@Fe$_{SAC}$-N$_4$/C and Co@Fe$_{SAC}$-N$_2$P/C show the main peak at around 2.44 Å attributed to Co-Co metallic bond, indicating that Co is a metal state (Fig. 2a) [34]. The Fe phase-corrected FT-EXAFS spectrum of Co@Fe$_{SAC}$-N$_4$/C shows a distance at 1.79 Å, indicating the existence of Fe-N coordination (Fig. 2b) [35]. However, after IL modification, the FT-EXAFS spectra exhibit two obvious peaks located at 1.78 and 2.22 Å, attributing to the nearest Fe-N and Fe-P coordination, indicating the existence of two Fe heteroatom bridge sites [36]. Additionally, the lack
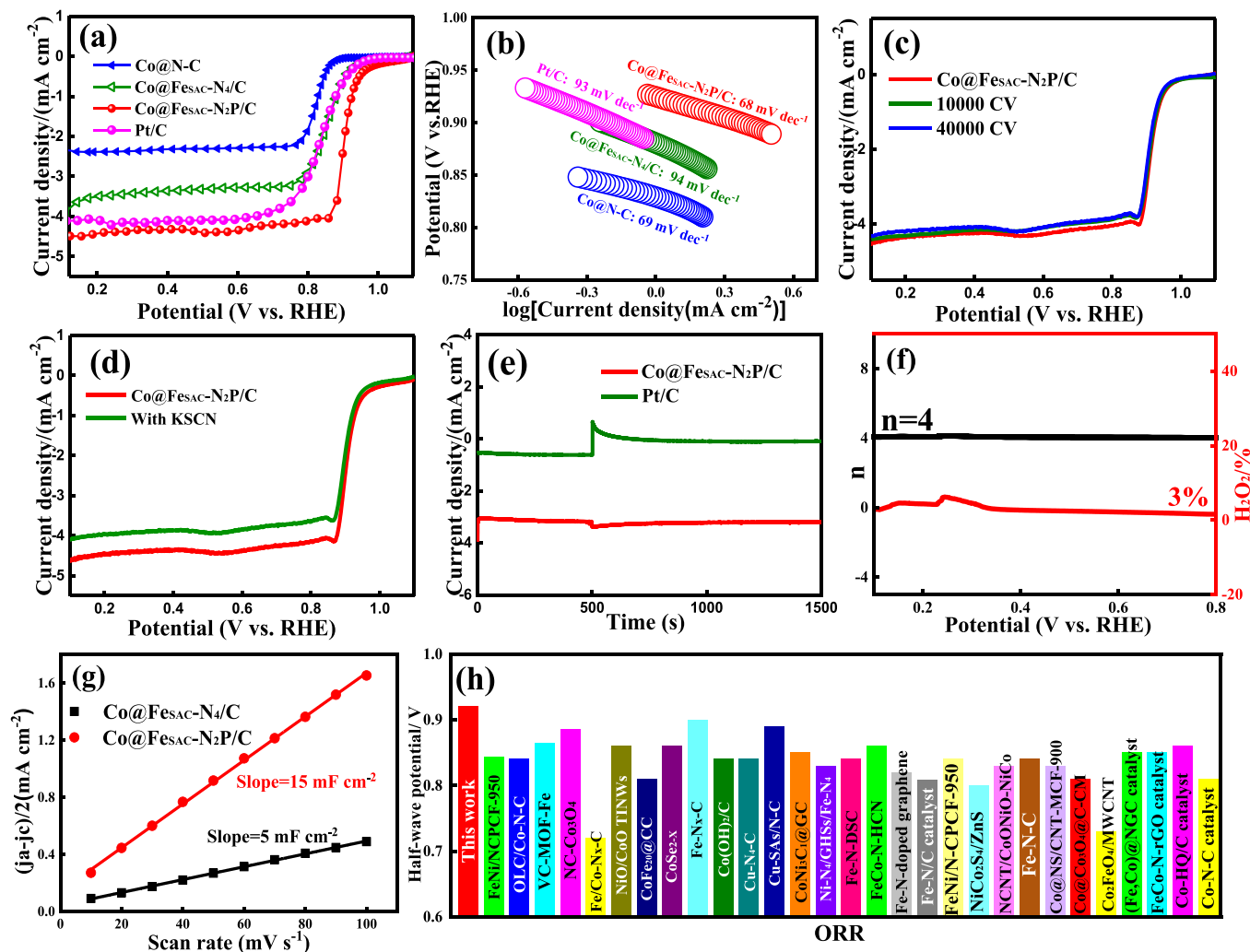
Fig. 3. a) ORR polarization curves, b) Tafel slope, c) LSV curves of Co@Fe$_{SAC}$-N$_2$P/C before and after 40,000 cycles, d) ORR performance of Co@Fe$_{SAC}$-N$_2$P/C before and after the add KSCN, e) Methanol resistance test, f) Peroxide percentage (H$_2$O$_2$%) and the corresponding number of electron transferred, g) The values of Cdl for Co@Fe$_{SAC}$-N$_4$/C and Co@Fe$_{SAC}$-N$_2$P/C, and h) Comparison of E$_{1/2}$ of Co@Fe$_{SAC}$-N$_2$P/C and the previously reported catalysts.

of Fe-Fe characteristic peak (2.46 Å) in Co@Fe$_{SAC}$-N$_4$/C and Co@Fe$_{SAC}$-N$_2$P/C indicates that Fe is the isolated single atoms in both two samples (Fig. 2b) [37]. In Fig. 2c, the Co@Fe$_{SAC}$-N$_2$P/C exhibits three scattering paths of Fe-N, Fe-P, and Fe-C bands.

The Fe K-edge XANES spectra reveal that the average oxidation state of Fe in Co@Fe$_{SAC}$-N$_4$/C closes to FePc, indicating a Fe^{2+} valence state [34]. And the line position (absorption edge) of Co@Fe$_{SAC}$-N$_2$P/C is between Fe foil and FePc, demonstrating the valence state of Fe in Co@Fe$_{SAC}$-N$_2$P/C is between Fe^0 and Fe^{2+} (Fig. S5b). Furthermore, to precisely determine the average oxidation state of Co@Fe$_{SAC}$-N$_2$P/C, the first derivative of Fe K-edge of Co@Fe$_{SAC}$-N$_2$P/C and the corresponding Fe foil and Fe$_2$O$_3$ references are obtained. Through the linear fitting calibration of the corresponding Fe foil (7113.08 eV) and Fe$_2$O$_3$ (7126.15 eV) references, the average oxidation state of the Co@Fe$_{SAC}$-N$_2$P/C (7121.64 eV) is determined to be 1.96 (Fig. 2d–e) [38]. To obtain structural parameters of Co@Fe$_{SAC}$-N$_4$/C and Co@Fe$_{SAC}$-N$_2$P/C, the least-squares EXAFS fitting analysis are conducted to extract quantitative structural for the Fe, and the corresponding coordination numbers are shown in Table S1 and Table S2. The best-fitting results reveal that the Fe in Co@Fe$_{SAC}$-N$_4$/C is coordinated with four N to constitute Fe-N$_4$ structure (Fig. S6a–b, Table S1). After IL modification, the best-fitting analyses clearly demonstrates that the two peak are ascribed to superimposition of Fe-N and Fe-P first-shell coordination (Figs. 2f, S6c, Table S2). And the Fe SACs are coordinated with two N

and one P atoms with the average bond lengths of 2.07 and 2.40 Å, respectively, which suggests a single-atom Fe-N$_2$P moiety (Table S2). Due to the high sensitivity of XANES spectrum to local coordination environment of the absorbing species, the XANES simulation is further performed to identify the atomic configuration [39]. The structural models under different coordination environments are established by DFT calculation, and the corresponding XANES spectra are also calculated (Figs. 2g, S7). And the spectra simulated by the Fe-N$_2$P model (Fe-N$_2$P-2) corresponded well to the XANES characteristics in the experiment from the above DFT calculations (Fig. 2g blue line, Fig. S7b) [39]. However, the other calculated spectra (Fe-N$_2$P-1) are distinctly different from the experimental results (Figs. 2g red line, S7a). The synergistic results of EXAFS and XANES clearly demonstrated the formation of single atoms Fe-N$_2$P moieties with specific configuration in the catalyst. In addition, the EXAFS wavelet transform (WT) analysis of Co@Fe$_{SAC}$-N$_2$P/C is conducted to directly demonstrate scattering path signal for Fe-N and Fe-P bonding, whereas a peak at 4.5 Å^{-1} belong to Fe-Fe coordination is not detected (Fig. 2h–j). These results further confirm that Fe exists in the form of Fe-N and Fe-P coordination in Co@FeSAC-N$_2$P/C catalyst. The SACs catalysts were investigated by electron paramagnetic resonance (EPR) to identify the unsaturated coordination. In Fig. S6d, a paramagnetic absorption signal at g = 2.02 could be attributed to anion vacancy [40]. Compared with Co@Fe$_{SAC}$-N$_4$/C, the signal intensity of Co@Fe$_{SAC}$-N$_2$P/C is increased,
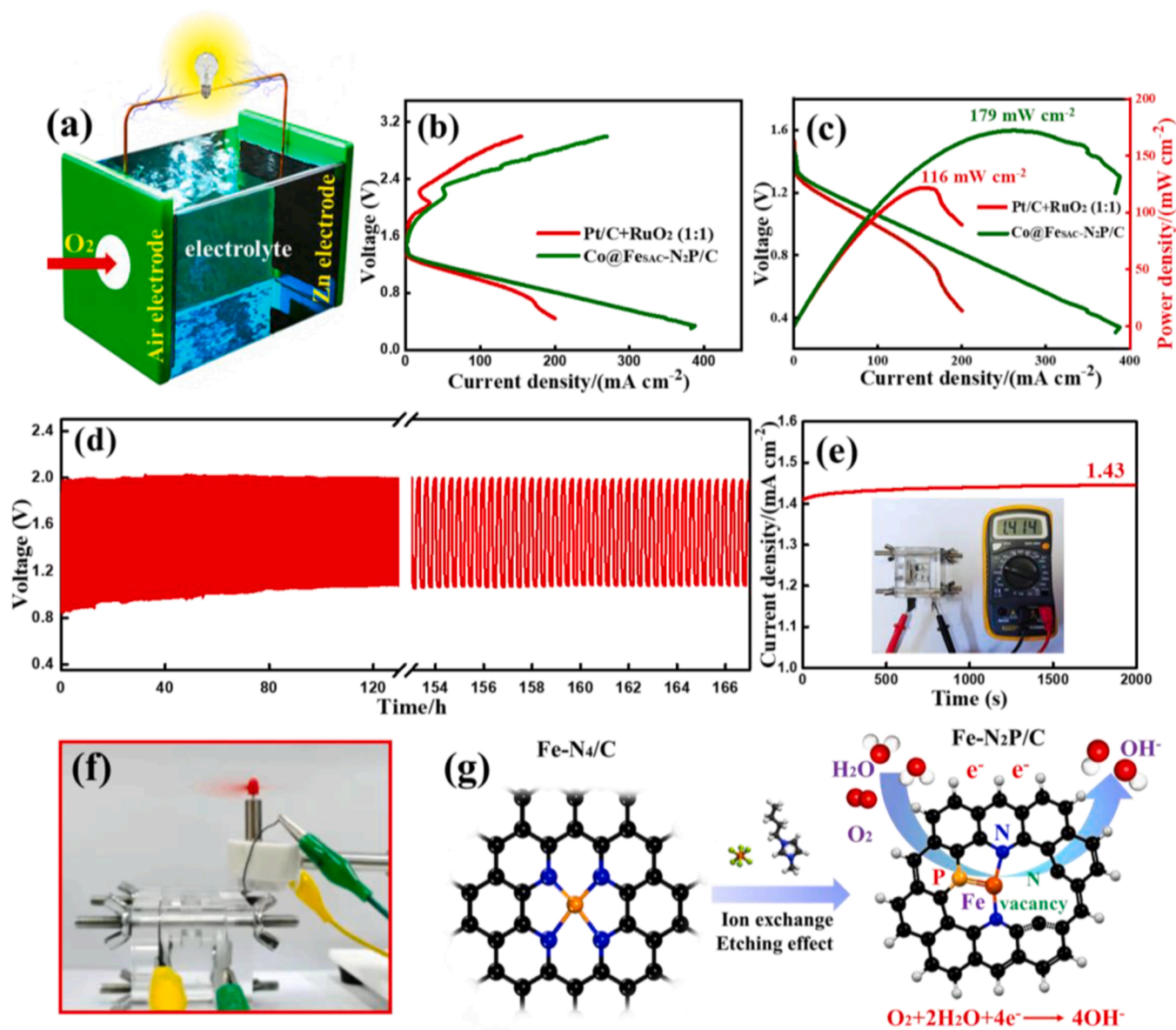
Fig. 4. a) Schematic diagram of Zn-air battery, b) charge-discharge polarization curves, and c) power density of Co@Fe$_{SAC}$-N$_2$P/C and Pt/C+RuO$_2$. d) discharge and charge cycling performance of Co@Fe$_{SAC}$-N$_2$P/C, e) open-circuit voltage of 1.43 V, and f) the fan powered by a Zn-air battery. g) schematic diagram of different coordination environments, and the four-electron transfer process of catalysts.

indicating that partial N vacancies were generated after IL immersion, corresponding to the results of XANES [41].

3.2. ORR catalytic performance

The rotating disk electrode (RDE) technique is employed to evaluate the ORR activity of Co@ /N-C, Co@Fe$_{SAC}$-N$_4$/C, Co@Fe$_{SAC}$-N$_2$P/C, and Pt/C in O$_2$-saturated 0.1 M KOH. As ferrocene and IL exert great effect on the electrocatalytic property of the Co@Fe$_{SAC}$-N$_4$/C, the ORR performance of the catalysts synthesized with different amount of ferrocene and IL are tested (Fig. S8). As the doping amount of ferrocene and IL is 3 mmol and 70 mg, respectively, the Co@Fe$_{SAC}$-N$_2$P/C catalyst exhibits the optimal activity, as demonstrated by the highest onset and half-wave potential (Fig. S8). From Fig. 3a, the Co@Fe$_{SAC}$-N$_2$P/C displays superior catalytic activity in terms of highest onset potential (E$_{onset}$, 0.97 V) and half-wave potential (E$_{1/2}$, 0.92 V), extremely over than those of Co@ / N-C (E$_{1/2}$ = 0.82 V), Co@Fe$_{SAC}$-N$_4$/C (E$_{1/2}$ = 0.86 V), Fe-N$_4$ (E$_{1/2}$ = 0.83 V) (Fig. S9a), and the benchmark Pt/C (E$_{1/2}$ = 0.85 V),

respectively. At the same time, the Tafel slope of Co@Fe$_{SAC}$-N$_2$P/C is 68 mV·dec^{-1}, lower than other contrast samples (Fig. 3b). Moreover, the electrochemical stability for the Co@Fe$_{SAC}$-N$_4$/C and Co@Fe$_{SAC}$-N$_2$P/C are assessed by CV in 0.1 M KOH. As shown in Fig. 3c, no obvious decrease in half-wave potential of Co@Fe$_{SAC}$-N$_2$P/C is observed even after 40,000 continuous cycles, while Co@Fe$_{SAC}$-N$_4$/C suffers obvious ORR performance degradation (Fig. S9b). After durability tests, the morphology of Co@Fe$_{SAC}$-N$_2$P/C sample still remains intact (Fig. S10d–f), while the surface of Co@Fe$_{SAC}$-N$_4$/C is seriously corroded by strong alkali solution (Fig. S10a–c). The above comparison indicates that the unsaturated heteroatom coordination structure and hydrophobic surface induced by ionic liquid modification can actually improve the ORR activity and stability. To further investigate the role of single Fe atom active sites in ORR, SCN-ions with strong affinity for Fe species were implanted into poison the SAC Fe-N$_2$P sites. Upon the addition of KSCN solution into 0.1 M KOH, the ORR performance of Co@Fe$_{SAC}$-N$_4$/ C is significantly reduced, clearly manifesting that the single Fe atom sites as the main active sites for ORR (Fig. S11) [42]. In addition, the
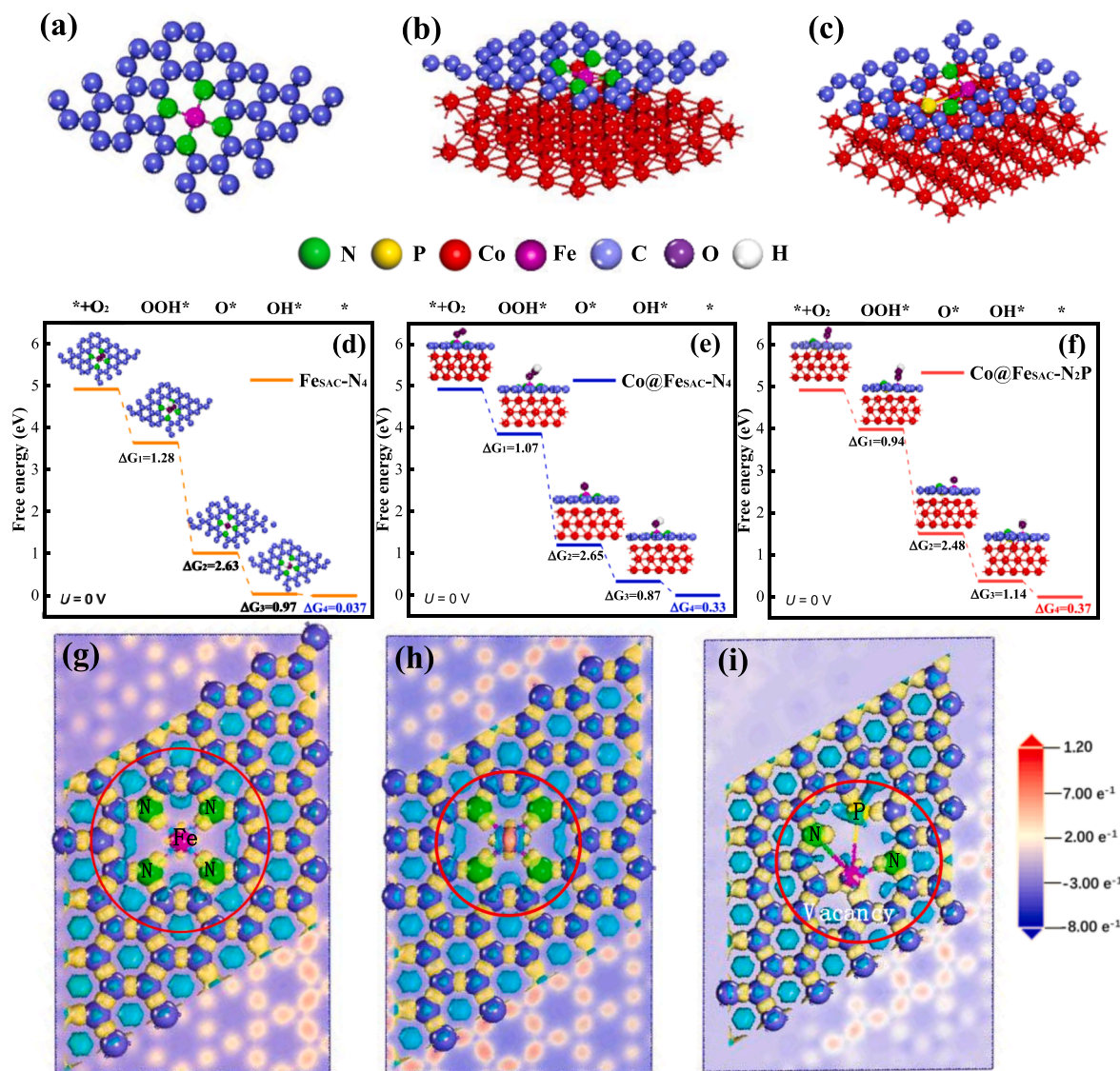
Fig. 5. The configurations of the adsorbed intermediates on a) Fe_{SAC}-N_4, b) Co@Fe_{SAC}-N_4, and c) Co@Fe_{SAC}-N_2P; d-f) Gibbs free energy change diagram of Fe-N_4, Co@Fe_{SAC}-N_4, and Co@Fe_{SAC}-N_2P; g-i) the calculated charge density distribution of Fe_{SAC}-N_4, Co@Fe_{SAC}-N_4, and Co@Fe_{SAC}-N_2P, respectively.

ORR activity remained high after the addition of KSCN, indicating that Co substance may also facilitate the ORR property. However, after IL modification, the half-wave potential of Co@Fe_{SAC}-N_2P/C remains unchanged and current density reduce only by 0.24 mA·cm^{-2} after the addition of KSCN (Fig. 3d). The above results show that the hydrophobically modified catalyst surface can protect the active site of the catalyst by repelled H_2O and alkaline electrolytes and improve the stability of the sample. The tolerance to methanol is a crucial factor for practical applications. As shown in Fig. 3e, Co@Fe_{SAC}-N_2P/C shows well methanol resistance compared to the Pt/C after methanol injection. The ORR pathway of Co@Fe_{SAC}-N_2P/C is evaluated by the RRDE measurements (Fig. S12). The yield of H_2O_2 for Co@Fe_{SAC}-N_2P/C is about ∼ 3%. The value of double-layer capacitance Correspondingly, Co@Fe_{SAC}-N_2P/C has a 4e reaction process with n = ∼ 4 (Fig. 3f) [43,44]. The value of double-layer capacitance (Cdl) is found to be 15 mF·cm^{-2} for Co@Fe_{SAC}-N_2P/C, higher than that of Co@Fe_{SAC}-N_4/C (5 mF·cm^{-2}), indicating the existence of N, P synergistic coordinated Fe single atom facilitates to increase the electrochemically active surface area (ESCA) (Fig. S14 and Fig. 3g). Furthermore, the ORR activity of Co@Fe_{SAC}-N_2P/C is comparable to those of various Fe/Co-N_x-C, Cu-N_4/C, and Fe-N_x-C in alkaline media, as listed in Fig. 3h and Table S3, exceeding

that of the commercial Pt/C catalyst and almost all non-precious ORR electrocatalysts.

3.3. Application of electrocatalyst in zinc-air battery

To demonstrate the practical application of Co@Fe_{SAC}-N_2P/C electrocatalysts in energy conversion devices, the Zn-air battery (ZABs) was constructed using Co@Fe_{SAC}-N_2P/C coated on carbon paper as air cathode, purity Zinc foil as the anode, and 6 M KOH as the electrolytes (Fig. 4a) [45,46]. According to the discharge polarization curves (Fig. 4b), the power density of Co@Fe_{SAC}-N_2P/C delivers a larger power density of 179 mW·cm^{-2}, which is much higher than Pt/C+IrO$_2$ (116 mW·cm^{-2}) (Fig. 4c). Furthermore, an open-circuit voltage of 1.43 V (Fig. 4e), which can power the electric fan to rotate rapidly (Fig. 4f). Strikingly, this battery based on Co@Fe_{SAC}-N_2P/C exhibits outstanding stability, as evidenced by more than 165 h (330 cycles) at 5.0 mA·cm^{-2} without obvious performance decay (Fig. 4d). Fig. 4g shows the reaction mechanism and four-electron transfer process of the catalyst.
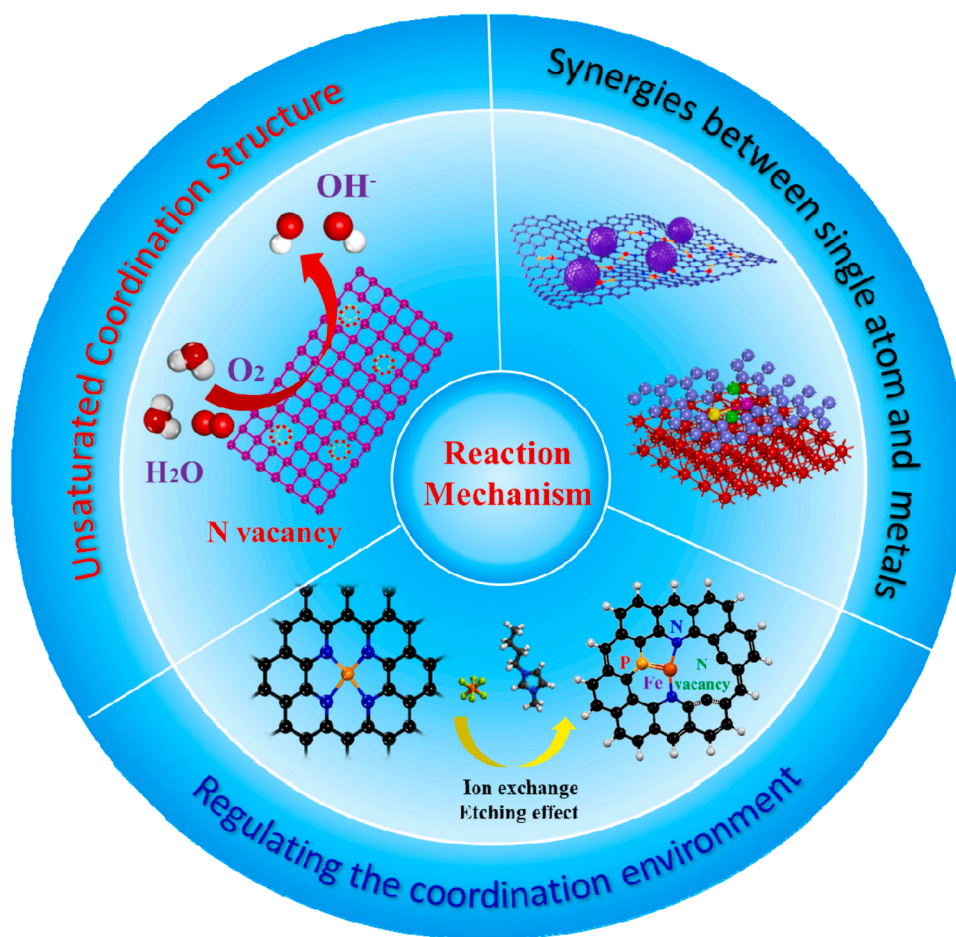
Scheme 1. Schematic diagram of catalytic performance over Co@Fe_{SAC}-N_2P/C.

3.4. DFT calculations

To gain the origin of the excellent ORR activity and kinetics of Co@Fe$_{SAC}$-N$_2$P/C, the DFT calculations were implemented for the ORR mechanism of bare Fe$_{SAC}$-N$_4$, Co@Fe$_{SAC}$-N$_4$, and Co@Fe$_{SAC}$-N$_2$P. In alkaline media, For ORR, the change of Gibbs free energy (G) of adsorbed intermediates (*O, *OH, *OOH) are closely related to the activity of the electrocatalyst [47,48]. The ORR processes and the optimized configuration involved in the intermediate in the Fe$_{SAC}$-N$_4$, Co@Fe$_{SAC}$-N$_4$, and Co@Fe$_{SAC}$-N$_2$P have been shown in Fig. 5a–c. Fig. 5d–f exhibits the Gibbs free energies (eV) for each reaction intermediates (*O, *OH, and *OOH) in ORR. The calculation indicates that all four elementary reaction pathways on Fe$_{SAC}$-N$_4$, Co@Fe$_{SAC}$-N$_4$, and Co@Fe$_{SAC}$-N$_2$P showed consistent downhill, corroborating exothermic reactions in ORR. Among of the four processes, the one with the smallest Gibbs free energy change ΔG is the rate-limited step, which is the rate-determining step for ORR [49,50]. The smallest ΔG_4 of the last electron transfer step (*OH + e$^-$ → * + OH$^-$) is the rate-limiting step, where the ΔG_4 values are calculated to be 0.037 V (Fe$_{SAC}$-N$_4$), 0.33 V (Co@Fe$_{SAC}$-N$_4$), and 0.37 V (Co@Fe$_{SAC}$-N$_2$P), suggesting that the ORR activities increase in the order of: Fe$_{SAC}$-N$_4$ < Co@Fe$_{SAC}$-N$_4$ < Co@Fe$_{SAC}$-N$_2$P. This is consistent with the experimental results. The structural diagrams in Fig. 5b and c show strong electron coupling between Co nanoparticles and carbon material, which facilitates electron transfer from Co nanoparticles to carbon material. Furthermore, the biggest energy change values of Co@Fe$_{SAC}$-N$_2$P was the second electron transfer step of *OOH + e$^-$ → *O + OH$^-$ with the ΔG_2 = 2.48 eV. In addition, overpotential (η) is a key index parameter to evaluate the ORR performance of electrocatalysts, which can be calculated using the formula of η = 1.23[V] - min[ΔG_i]/e, and ΔG_i is the minimum Gibbs free energy differences [51,52]. Therefore, the overpotential on Co@Fe$_{SAC}$-N$_2$P is 0.86 V, lower than that of 0.90 V of Co@Fe$_{SAC}$-N$_4$ and 1.19 V of Fe$_{SAC}$-N$_4$, respectively. Therefore, compared with Fe$_{SAC}$-N$_4$ and Co@Fe$_{SAC}$-N$_4$, the electronic structure of the Co@Fe$_{SAC}$-N$_2$P catalyst has a significant influence on the rate-determining step for ORR. The differential charge density of Fe-N$_4$, Co@Fe$_{SAC}$-N$_4$, and Co@Fe$_{SAC}$-N$_2$P were also computed (Fig. 5g–i). The yellow and wathet blue regions represent electrons gained and electrons lost, respectively. Electron density difference analysis reveals an effective electron transfer from N vacancy to Fe. The N vacancy in Co@Fe$_{SAC}$-N$_2$P is an electron donor (yellow region), which can donate electrons to the neighboring Fe atom. The N vacancy can tailor the electronic structure of the metal atoms and alter the charge distribution at the coordination structures, leading to higher electron density around Fe active sites [53–55]. This means that the valence of Fe in Co@Fe$_{SAC}$-N$_2$P is lower than that in Co@Fe$_{SAC}$-N$_4$, which is consistent well with XANES experimental results. Particularly, the unsaturated coordination (N vacancy), the coordination states of P atoms, and the strong electron coupling between Co and carbon material play critical roles in reducing the reaction barrier, and promotes the ORR dynamics.

The as-prepared Co@Fe$_{SAC}$-N$_2$P/C catalyst exhibits superior ORR activity and long-term durability, which maybe attribute the following aspects: (1) The construction of Fe-N$_2$P unsaturated coordination structure can break the symmetry of electronic density, thus speeding up the ORR kinetics and performance. (2) The hydrophobic surface can maintain a higher O$_2$ concentration at the catalyst interface, which can increase residence time and trial frequency of ORR and enhance the activity. (3) Modifying the catalyst surface to be hydrophobic can

protect the active site of the catalyst by repelled H_2O and alkaline electrolytes and improve the stability of the sample. (4) The N vacancy caused by Co@Fe$_{SAC}$-N$_2$P/C mixed unsaturated coordination can accelerate electron transfer, thus enhanced ORR performance (Scheme 1).

4. Conclusion

In conclusion, we have developed a facile ionic liquid modification strategy to obtain Co@Fe$_{SAC}$-N$_2$P/C mixed unsaturated coordination, achieving the function of regulating the coordination environment and hydrophobicity of the Co@Fe$_{SAC}$-N$_4$/C catalyst simultaneously. This approach also averts the complex changes in the previous long-term pyrolysis method. The Co@Fe$_{SAC}$-N$_2$P/C with unsaturated coordination and hydrophobic surface exhibits superior ORR performance with a half-wave potential of 0.92 V and a long stability with 40,000 cycles, exceeding that of the commercial Pt/C catalyst and almost all non-precious ORR electrocatalysts. This study provides a convenient and effective approach for accurately controlling the coordination electronic structure and interface environment of SACs and optimizing ORR performance at room temperature.

CRediT authorship contribution statement

Jing Sun: Methodology, Investigation, Data curation, Writing – original draft. **Hui Xue:** Methodology, Investigation, Data curation, Writing – original draft. **Lanlu Lu:** Methodology, Formal analysis, Data curation, Writing – original draft. **Mingbin Gao:** Software, Investigation, Data curation. **Niankun Guo:** Validation, Investigation. **Tianshan Song:** Validation, Investigation. **Hongliang Dong:** Formal analysis, Investigation, Visualization. **Jiangwei Zhang:** Conceptualization, Methodology, Software, Investigation, Writing – review & editing, Visualization, Supervision, Project administration, Funding acquisition. **Qin Wang:** Conceptualization, Methodology, Resources, Writing – review & editing, Supervision, Project administration, Funding acquisition. **Limin Wu:** Conceptualization, Writing – Review & editing, Supervision, Project administration.

Declaration of Competing Interest

The authors declare that they have no known competing financial interests or personal relationships that could have appeared to influence the work reported in this paper.

Appendix A. Supporting information

Supplementary data associated with this article can be found in the online version at doi:10.1016/j.apcatb.2022.121429.

References

[1] A. Wang, J. Li, T. Zhang, Heterogeneous single-atom catalysis, Nat. Rev. Chem. 2 (2018) 65–81.

[2] Y. Chen, S. Ji, C. Chen, Q. Peng, D. Wang, Y. Li, Single-atom catalysts: synthetic strategies and electrochemical applications, Joule 2 (2018) 1242–1264.

[3] J. Wang, W. Fang, Y. Hu, Y. Zhang, J. Dang, Y. Wu, B. Chen, H. Zhao, Z. Li, Single atom Ru doping 2H-MoS$_2$ as highly efficient hydrogen evolution reaction electrocatalyst in a wide pH range, Appl. Catal. B Environ. 298 (2021), 120490.

[4] B. Wang, Y. Ye, L. Xu, Y. Quan, W. Wei, W. Zhu, H. Li, J. Xia, Space-confined yolkshell construction of Fe$_3$O$_4$ nanoparticles inside N-doped hollow mesoporous carbon spheres as bifunctional electrocatalysts for long-term rechargeable zinc–air batteries, Adv. Funct. Mater. 30 (2020), 2005834.

[5] L. Liu, A. Corma, A. metal catalysts for heterogeneous catalysis: from single atoms to nanoclusters and nanoparticles, Chem. Rev. 118 (2018) 4981–5079.

[6] C. Wang, L. Jin, H. Shang, H. Xu, Y. Shiraishi, Y. Du, Advances in engineering RuO$_2$ electrocatalysts towards oxygen evolution reaction, Chin. Chem. Lett. 32 (2021) 2108–2116.

[7] Q. Zhang, F. Luo, X. Long, X. Yu, K. Qu, Z. Yang, N, P doped carbon nanotubes confined WN-Ni Mott-Schottky heterogeneous electrocatalyst for water splitting and rechargeable zinc-air batteries, Appl. Catal. B Environ. 298 (2021), 120511.

[8] J. Gu, C.S. Hsu, L. Bai, H.M. Chen, X. Hu, Atomically dispersed Fe^{3+} sites catalyze efficient CO$_2$ electroreduction to CO, Science 364 (2019) 1091–1094.

[9] J. Meng, C. Niu, L. Xu, J. Li, X. Liu, X. Wang, Y. Wu, X. Wen, Q. Li, Z. Zhu, D. Zhao, L. Mai, General oriented formation of carbon nanotubes from metal–organic frameworks, J. Am. Chem. Soc. 139 (2017) 8212–8221.

[10] Y. Feng, H. Wang, S. Zhang, Y. Zhao, J. Gao, Y. Zheng, P. Zhao, Z. Zhang, M. J. Zaworotko, P. Cheng, S. Ma, Y. Chen, Antibodies@MOFs: an in vitro protective coating for preparation and storage of biopharmaceuticals, Adv. Mater. 31 (2019), 1805148.

[11] X. Zhao, Y. Wang, D.S. Li, X. Bu, P. Feng, Metal–organic frameworks for separation, Adv. Mater. 30 (2018), 1705189.

[12] X. Wang, H. Zhang, H. Lin, S. Gupta, C. Wang, Z. Tao, H. Fu, T. Wang, J. Zheng, G. Wu, X. Li, Directly converting Fe-doped metal–organic frameworks into highly active and stable Fe-N-C catalysts for oxygen reduction in acid, Nano Energy 25 (2016) 110–119.

[13] J. Zhang, Y. Zhao, C. Chen, Y.C. Huang, C.L. Dong, C.J. Chen, R.S. Liu, C. Wang, K. Yan, Y. Li, G. Wang, Tuning the coordination environment in single-atom catalysts to achieve highly efficient oxygen reduction reactions, J. Am. Chem. Soc. 141 (2019) 20118–20126.

[14] B. Wang, Y. Ye, L. Xu, Y. Quan, W. Wei, W. Zhu, H. Li, J. Xia, Space-confined yolkshell construction of Fe$_3$O$_4$ nanoparticles inside N-doped hollow mesoporous carbon spheres as bifunctional electrocatalysts for long-term rechargeable zinc–air batteries, Adv. Funct. Mater. 30 (2020), 2005834.

[15] Y. Gong, L. Jiao, Y. Qian, C. Pan, L. Zheng, X. Cai, B. Liu, S.H. Yu, H. Jiang, Adv. Mater. 31 (2019), 1900592.

[16] T. Zheng, K. Jiang, H. Wang, Recent advances in electrochemical CO$_2$-to-CO conversion on heterogeneous catalysts, Adv. Mater. 30 (2018), 1802066.

[17] Z. Wang, J. Ang, J. Liu, X.Y.D. Ma, J. Kong, Y. Zhang, T. Yan, X. Lu, FeNi alloys encapsulated in N-doped CNTs-tangled porous carbon fibers as highly efficient and durable bifunctional oxygen electrocatalyst for rechargeable zinc-air battery, Appl. Catal. B Environ. 263 (2020), 118344.

[18] H. Shang, T. Wang, Jia Pei, Z. Jiang, D. Zhou, Y. Wang, H. Li, J. Dong, Z. Zhuang, W. Chen, D. Wang, J. Zhang, Y. Li, Design of a single-atom indium$^{\delta+}$-N$_4$ interface for efficient electroreduction of CO$_2$ to formate, Angew. Chem. Int. Ed. 59 (2020) 22465–22469.

[19] C. Wang, H. Shang, J. Li, Y. Wang, H. Xu, C. Wang, J. Guo, Y. Du, Ultralow Ru doping induced interface engineering in MOF derived ruthenium-cobalt oxide hollow nanobox for efficient water oxidation electrocatalysis, Chem. Eng. J. 420 (2021), 129805.

[20] Y. Tan, C. Xu, G. Chen, N. Zheng, Q. Xie, A graphene–platinum nanoparticles–ionic liquid composite catalyst for methanol-tolerant oxygen reduction reaction, Energy Environ. Sci. 5 (2012) 6923–6927.

[21] R. Jinnouchi, A.B. Anderson, Electronic structure calculations of liquid-solid interfaces: Combination of density functional theory and modified Poisson-Boltzmann theory, Phys. Rev. B 77 (2008), 245417.

[22] G.R. Zhang, M. Munoz, B.J.M. Etzold, Accelerating oxygen-reduction catalysts through preventing poisoning with non-reactive species by using hydrophobic ionic liquids, Angew. Chem. Int. Ed. 55 (2016) 2257–2261.

[23] J. Sun, N. Guo, Z. Shao, K. Huang, Y. Li, F. He, Q. Wang, A facile strategy to construct amorphous spinel-based electrocatalysts with massive oxygen vacancies using ionic liquid dopant, Adv. Energy Mater. 8 (2018), 1800980.

[24] L. Zhang, J.M.T.A. Fischer, Y. Jia, X. Yan, W. Xu, X. Wang, J. Chen, D. Yang, H. Liu, L. Zhuang, M. Hankel, D.J. Searles, K. Huang, S. Feng, C.L. Brown, X. Yao, Coordination of atomic Co-Pt coupling species at carbon defects as active sites for oxygen reduction reaction, J. Am. Chem. Soc. 140 (2018) 10757–10763.

[25] L. Zhuang, Y. Jia, H. Liu, X. Wang, R.K. Hocking, H. Liu, J. Chen, L. Ge, L. Zhang, M. Li, C.L. Dong, Y.C. Huang, S. Shen, D. Yang, Z. Zhu, X. Yao, Defect-induced Pt–Co–Se coordinated sites with highly asymmetrical electronic distribution for boosting oxygen-involving electrocatalysis, Adv. Mater. 31 (2019), 1805581.

[26] S. Yuan, L.L. Cui, Z. Dou, X. Ge, X. He, W. Zhang, T. Asefa, Nonprecious bimetallic sites coordinated on N-doped carbons with efficient and durable catalytic activity for oxygen reduction, Small 16 (2020), 2000742.

[27] C.Y. Su, H. Cheng, W. Li, Z.Q. Liu, N. Li, Z. Hou, F.Q. Bai, H.X. Zhang, T.Y. Ma, Atomic modulation of FeCo–nitrogen–carbon bifunctional oxygen electrodes for

rechargeable and flexible all-solid-state zinc–air battery, Adv. Energy Mater. 7 (2017), 1602420.

[28] J. Sun, H. Xue, N. Guo, T. Song, Y. Hao, J. Sun, J. Zhang, Q. Wang, Synergetic metal defect and surface chemical reconstruction into NiCo$_2$S$_4$/ZnS heterojunction to achieve outstanding oxygen evolution performance, Angew. Chem. Int. Ed. 60 (2021) 19435–19441.

[29] B. Liu, X. Li, L. Xiao, L. Zhou, Q. Xu, J. Weng, J. Xu, Adaptive bifunctional electrocatalyst of amorphous CoFe Oxide @ 2D black phosphorus for overall water splitting, Angew. Chem. Int. Ed. 59 (2020) 21106–21113.

[30] M. Tong, F. Sun, Y. Xie, Y. Wang, Y. Yang, C. Tian, L. Wang, H. Fu, Operando cooperated catalytic mechanism of atomically dispersed CuN$_4$ and ZnN$_4$ for promoting oxygen reduction reaction, Angew. Chem. Int. Ed. 60 (2021) 14005–14012.

[31] T. Liu, J. Mou, Z. Wu, C. Lv, J. Huang, M. Liu, A facile and scalable strategy for fabrication of superior bifunctional freestanding air electrodes for flexible zinc–air batteries, Adv. Funct. Mater. 30 (2020) 2003407–2003416.

[32] X. Ji, C. Cheng, Z. Zang, L. Li, X. Li, Y. Cheng, X. Yang, X. Yu, Z. Lu, X. Zhang, H. Liu, Ultrathin and porous &-FeOOH modified Ni$_3$S$_2$ 3D heterostructure nanosheets with excellent alkaline overall water splitting performance, J. Mater. Chem. A 8 (2020) 21199–21207.

[33] D. Qi, Y. Liu, M. Hu, X. Peng, Y. Qiu, S. Zhang, W. Liu, H. Li, G. Hu, L. Zhuo, Y. Qin, J. He, G. Qi, J. Sun, J. Luo, X. Liu, Engineering atomic sites via adjacent dual-metal sub-nanoclusters for efficient oxygen reduction reaction and Zn-air battery, Small 16 (2020), 2004855.

[34] L. Jiao, R. Zhang, G. Wan, W. Yang, X. Wan, H. Zhou, J. Shui, S.H. Yu, H.L. Jiang, Nanocasting SiO$_2$ into metal–organic frameworks imparts dual protection to high-loading Fe single-atom electrocatalysts, Nat. Commun. 11 (2020) 2831.

[35] X. Han, X. Ling, D. Yu, D. Xie, L. Li, S. Peng, C. Zhong, N. Zhao, Y. Deng, W. Hu, Atomically dispersed binary Co-Ni sites in nitrogen-doped hollow carbon nanocubes for reversible oxygen reduction and evolution, Adv. Mater. 31 (2019), 1905622.

[36] Y. Chen, R. Gao, S. Ji, H. Li, K. Tang, P. Jiang, H. Hu, Z. Zhang, H. Hao, Q. Qu, X. Liang, W. Chen, J. Dong, D. Wang, Y. Li, Atomic-level modulation of electronic density at cobalt single-atom sites derived from metal–organic frameworks: enhanced oxygen reduction performance, Angew. Chem. Int. Ed. 60 (2021) 3212–3221.

[37] L. Jiao, W. Yang, G. Wan, R. Zhang, X. Zheng, H. Zhou, S.H. Yu, H.L. Jiang, Single-atom electrocatalysts from multivariate metal–organic frameworks for highly selective reduction of CO$_2$ at low pressures, Angew. Chem. Int. Ed. 59 (2020) 20589–20595.

[38] L.J. Liu, J.W. Zhang, M. Asad, Z.Y. Wang, S.Q. Zang, T.C.W. Mak, A high-nuclearity Cu^I/Cu^{II} nanocluster catalyst for phenol degradation, Chem. Commun. 57 (2021) 5586–5589.

[39] T. Cui, L. Ma, S. Wang, C. Ye, X. Liang, Z. Zhang, G. Meng, L. Zheng, H.S. Hu, J. Zhang, H. Duan, D. Wang, Y. Li, Atomically dispersed Pt–N$_3$C$_1$ sites enabling efficient and selective electrocatalytic c–c bond cleavage in lignin models under ambient conditions, J. Am. Chem. Soc. 143 (2021) 9429–9439.

[40] H. Wang, Z. Li, Y. Li, B. Yang, J. Chen, L. Lei, S. Wang, Y. Hou, An exfoliated iron phosphorus trisulfide nanosheet with rich sulfur vacancy for efficient dinitrogen fixation and Zn-N$_2$ battery, Nano Energy 81 (2021), 105613.

[41] Y.N. Gong, W. Zhong, Y. Li, Y. Qiu, L. Zheng, J. Jiang, H.L. Jiang, Regulating photocatalysis by spin-state manipulation of cobalt in covalent organic frameworks, J. Am. Chem. Soc. 142 (2020) 16723–16731.

[42] J.D. Yi, R. Xu, Q. Wu, T. Zhang, K.-T. Zang, J. Luo, Y.L. Liang, Y.B. Huang, R. Cao, Atomically dispersed iron-nitrogen active sites within porphyrinic triazine-based frameworks for oxygen reduction reaction in both alkaline and acidic media, ACS Energy Lett. 3 (2018) 883–889.

[43] J. Zhang, L. Yu, Y. Chen, X.F. Lu, S. Gao, X.W.D. Lou, Designed formation of double-shelled Ni–Fe layered-double-hydroxide nanocages for efficient oxygen evolution reaction, Adv. Mater. 32 (2020), 1906432.

[44] G. Chen, P. Liu, Z. Liao, F. Sun, Y. He, H. Zhong, T. Zhang, E. Zschech, M. Chen, G. Wu, J. Zhang, X. Feng, Zinc-mediated template synthesis of Fe-N-C electrocatalysts with densely accessible Fe-N$_X$ active sites for efficient oxygen reduction, Adv. Mater. 32 (2020) 1907399–1907406.

[45] H. Li, Q. Li, P. Wen, T.B. Williams, S. Adhikari, C. Dun, C. Lu, D. Itanze, L. Jiang, D. L. Carroll, Colloidal cobalt phosphide nanocrystals as trifunctional electrocatalysts for overall water splitting powered by a zinc–air battery, Adv. Mater. 30 (2018), 1705796.

[46] Y. Wang, N. Xu, R. He, L. Peng, D. Cai, J. Qiao, Large-scale defect-engineering tailored tri-doped graphene as a metal-free bifunctional catalyst for superior electrocatalytic oxygen reaction in rechargeable Zn-air battery, Appl. Catal. B Environ. 285 (2021), 119811.

[47] J.K. Nørskov, J. Rossmeisl, A. Logadottir, L. Lindqvist, J.R. Kitchin, T. Bligaard, H. Jonsson, Origin of the overpotential for oxygen reduction at a fuel-cell cathode, J. Phys. Chem. B 108 (2004) 17886–17892.

[48] H. Xu, D. Cheng, D. Cao, X.C. Zeng, A universal principle for a rational design of single-atom electrocatalysts, Nat. Catal. 1 (2018) 339–348.

[49] M. Xiao, L. Gao, Y. Wang, X. Wang, J. Zhu, Z. Jin, C. Liu, H. Chen, G. Li, J. Ge, Q. He, Z. Wu, Z. Chen, W. Xing, Engineering energy level of metal center: Ru single-atom site for efficient and durable oxygen reduction catalysis, J. Am. Chem. Soc. 141 (2019) 19800–19806.

[50] X. Zhao, X. Liu, B. Huang, P. Wang, Y. Pei, Hydroxyl group modification improves the electrocatalytic ORR and OER activity of graphene supported single and bimetal atomic catalysts (Ni, Co, and Fe), J. Mater. Chem. A 7 (2019) 24583–24593.

[51] T. Liu, J. Mou, Z. Wu, C. Lv, J. Huang, M. Liu, A facile and scalable strategy for fabrication of superior bifunctional freestanding air electrodes for flexible zinc–air batteries, Adv. Funct. Mater. 30 (2020) 2003407–2003416.

[52] N. Ran, W. Qiu, E. Song, Y. Wang, X. Zhao, Z. Liu, J. Liu, Bond electronegativity as hydrogen evolution reaction catalyst descriptor for transition metal (TM= Mo, W) dichalcogenides, Chem. Mater. 32 (2020) 1224–1234.

[53] C. Wang, H. Shang, H. Xu, Y. Du, Nanoboxes endow non-noble-metal-based electrocatalysts with high efficiency for overall water splitting, J. Mater. Chem. A 9 (2021) 857–874.

[54] X. Wang, Y. Jia, X. Mao, D. Liu, W. He, J. Li, J. Liu, X. Yan, J. Chen, L. Song, A. Du, X. Yao, Edge-rich Fe−N$_4$ active sites in defective carbon for oxygen reduction catalysis, Adv. Mater. 32 (2020), 2000966.

[55] D. Li, B. Wang, X. Long, W. Xu, Y. Xia, D. Yang, X. Yao, Controlled asymmetric charge distribution of active centers in conjugated polymers for oxygen reduction, Angew. Chem. Int. Ed. 60 (2021) 26483.